Official journal of the CIOMP 2047-7538
www.nature.com/lsa

ARTICLE Open Access

High efficiency pure blue perovskite quantum dot light-emitting diodes based on formamidinium manipulating carrier dynamics and electron state filling

Long Gao[1], Yilin Zhang[1], Lijie Gou[1], Qian Wang[1], Meng Wang[1], Weitao Zheng[1], Yinghui Wang[2], Hin-Lap Yip[3,4,5]✉ and Jiaqi Zhang[1]✉

Abstract

Achieving high efficiency and stable pure blue colloidal perovskite quantum dot (QD) light-emitting diodes (LEDs) is still an enormous challenge because blue emitters typically exhibit high defect density, low photoluminescence quantum yield (PLQY) and easy phase dissociation. Herein, an organic cation composition modification strategy is used to synthesize high-performance pure blue perovskite quantum dots at room temperature. The synthesized FA-$CsPb(Cl_{0.5}Br_{0.5})_3$ QDs show a bright photoluminescence with a high PLQY (65%), which is 6 times higher than the undoped samples. In addition, the photophysical properties of the FA cation doping was deeply illustrated through carrier dynamics and first principal calculation, which show lower defects, longer lifetime, and more reasonable band gap structure than undoped emitters. Consequently, pure blue FA-$CsPb(Cl_{0.5}Br_{0.5})_3$ QDs light-emitting devices were fabricated and presented a maximum luminance of 1452 cd m^{-2}, and an external quantum efficiency of 5.01 % with an emission at 474 nm. The excellent photoelectric properties mainly originate from the enhanced blue QDs emitter and effective charge injection and exciton radiation. Our finding underscores this easy and feasible room temperature doping approach as an alternative strategy to blue perovskite QD LED development.

Introduction

Perovskite halides, as a type of emerging semiconducting materials, exhibit outstanding optoelectronic properties, such as easily tunable optical bandgaps, high charge carrier mobility and long carrier diffusion length[1–5]. Benefiting from these characteristics, perovskite-based light-emitting diodes (PeLEDs) are considered as an alternative medium for high-efficiency solid-state lighting and panel display. However, the PLQYs of blue perovskite emitters, especially pure blue emission, are far behind green and red counterparts which EQEs of corresponding LEDs have both overtook 20%[6,7]. To achieve high-efficiency and high-luminance blue LEDs, devices with 3-dimensional (3D), 2D, and quasi-2D perovskites films of mixed-Cl/Br halides have been developed[8–10]. These films improve the stability of excitons and enhance the energy transfer by designing multiple-quantum-well and multi-cation-doped structure. The best-EQE device is 11.7% with an emission peak at 488 nm[11] and 13.8 % at 496 nm[12] so far. However, instead of thin films, perovskite QDs as emitters also show great potential in blue LEDs because of their high photoluminescence quantum yield (PLQY), strong quantum confinement effect, and high monochromaticity. Consequently, the development of blue QD emitters is still a key approach to enhance the performance of blue PeLEDs.

Correspondence: Hin-Lap Yip (a.yip@cityu.edu.hk) or
Jiaqi Zhang (zhangjiaqi@jlu.edu.cn)
[1]College of Materials Science and Engineering, Key Laboratory of Automobile Materials, Ministry of Education, Jilin University, Changchun 130012, China
[2]Femtosecond Laser laboratory, Key Laboratory of Physics and Technology for Advanced Batteries, Ministry of Education, College of Physics, Jilin University, Changchun 130012, China
Full list of author information is available at the end of the article

In 2014, the first QD-based PeLED was reported and the blue-emitting devices with Br and Cl mixed QDs were achieved with an EQE of 0.07%[13]. Then, various approaches have been employed to modify blue perovskite QDs. Ion doping has been proven a valid approach through altering the energy structure of perovskite QDs. In general, bivalent Mn^{2+}, Sn^{2+}, Cd^{2+}, Zn^{2+} and Cu^{2+}, trivalent lanthanide metal ions were often employed as B site dopants in blue perovskite QDs[14–17]. For example, the blue-emitting LED with Ni^{2+} doped $CsPbX_3$ emitting at 470 nm exhibited an EQE of 2.4%[18]. In addition, a multiple-cation doping strategy, i.e., simultaneous doping of A and B sites by inorganic cations into $CsPb(Br_xCl_{3-x})$, achieved high PLQY and an EQE of 2.14% for blue QD LEDs[19]. Apart from those, acid-etching small-sized QDs with low vacancy defect density and a maximum EQE value of 4.7% was realized through quantum-confined all-bromide perovskite QDs[20].

Instead of inorganic cation doping, organic cation doping is another effective strategy to manifest blue QD emitters. Organic doping could improve the thermal, moisture, and chemical stability of QDs[21–23]. Compared with all-inorganic Cs-based perovskite QDs, partial organic cation doping may form a more stable crystal structure. For example, FA cations, a doping method for perovskite solar cells and LEDs, could tune the perovskite tolerance factor close to 1, which improves the structure stability and suppresses the ion migration. However, excellent blue QDs with FA cation doping still lack of in-depth study especially in the room temperature synthesis which currently is the most up-and-coming route for catering large-scale synthesis and commercial application of perovskite QDs.

Herein, we comprehensively study the mechanism of FA cation doped blue QDs and achieve high-efficiency pure blue QD LEDs. Formamidine acetate (FAAc) was added as a precursor for the emitters. It can strongly improve the quality of QDs to reduce defect density and the nonradiative recombination. Furtherly, FA cations affect band-edge structure and enhance the interaction of organic cations and Pb-Br octahedron frameworks. The PLQY of pure blue perovskite QDs is improved from 10% (undoped) to 65% (FA doping). The substitution manipulates the crystal growth process, grain size, carrier injection barrier, and reduces defects in perovskite QDs. Finally, we realize blue perovskite QD LEDs, which has strong EL emission peak at 474 nm corresponding color coordinates of (0.113, 0.101). And, the optimized LEDs obtained a maximum value of brightness and EQE of 1452 cd m^{-2} and 5.01%, respectively. The LEDs exhibit a T_{50} lifetime of 1056 s with an initial brightness of 100 cd m^{-2}. FA cation doping is clarified to increase hot carrier relaxation and decrease nonradiative recombination by transient absorption spectroscopy. Density functional theory (DFT) calculations also elucidate that FA cations influence the state density of electrons in valence band (VB) and also the band structure, which eventually improves carrier injection.

Results

Structure characterization

Here, the microstructure of synthetized blue perovskite QDs via room temperature ligand assisted reprecipitation method (the details are shown in Experimental Section) is shown in Fig. 1. The transmission electron microscopy (TEM) images exhibit cubic QDs of ~11 nm for all undoped and FA-doped $CsPb(Cl_{0.5}Br_{0.5})_3$ QDs (Fig. 1a–e). The insets of narrower grain size distribution statistics further demonstrate the better uniformity of the cubic phase as more FA cations are added. This is mainly attributed to that the FA cations could adjust crystal framework. Clear lattice fringes were observed (Figs. 1f and S1), and the interplanar spacing of the (200) plane expands apparently from 2.60 to 2.71 Å with the adding FA cation increasing from 0 to 0.2 M, which indicates that FA cations were doped into the lattice. The schematic crystalline structure of $CsPb(Cl_{0.5}Br_{0.5})_3$ QDs is illustrated in Fig. 1g, where FA and Cs cations occupy the same spacing sites.

X-ray diffraction (XRD) and TEM measurements were conducted to explore the effect of FA cations on the structural properties of QDs. All samples show obvious diffraction peaks around $2\theta = 15.7°$, 22.3°, 31.6°, 35.2°, 38.8°, and 45.2°, corresponding to the (100), (110), (200), (210), (211), and (220) crystal planes of the cubic $CsPb(Br/Cl)_3$ phase, respectively (Fig. 1h). No extra diffraction peak can be observed in the FA cation doped samples, suggesting that FA^+ was incorporated into perovskite lattices. When the added FA cations reached 100%, the (100) diffraction peak decreases to 14.8° (Fig. S2). Also, the shift of diffraction peaks toward a lower angle suggests that the FA cations can cause lattice expansion, which is mainly due to the substitution of the smaller Cs^+ (1.81 Å) by larger FA^+ (2.79 Å)[24]. (200) plane was extracted as an example, in which a 0.36° shift toward a lower angle was observed with increasing FA^+. In addition, Cs^+ ions cause harmful shrinkage deformation of four coordination octahedrons ($[PbX_6]^{4-}$), which can be corrected by the doping of larger FA cations. However, excessive FA^+ ions can cause angle increase of two adjacent coordinating octahedra (> 180°). Here, the mechanism of defect healing by FA doping could be ascribed to lattice modulation of the distortion of $[PbX_6]^{4-}$. Figure 1h also displays that crystal growth tendency is distinctly affected by FA cation adding. FA^+ doped QDs realize the manipulation of crystal orientation along (100) crystal plane, which benefits to the light emission[25].

Photoluminescence studies and compositional analysis

Figure 2 shows the optical properties of the pristine and FA^+-doped $CsPb(Cl_{0.5}Br_{0.5})_3$ QDs. Compared with the

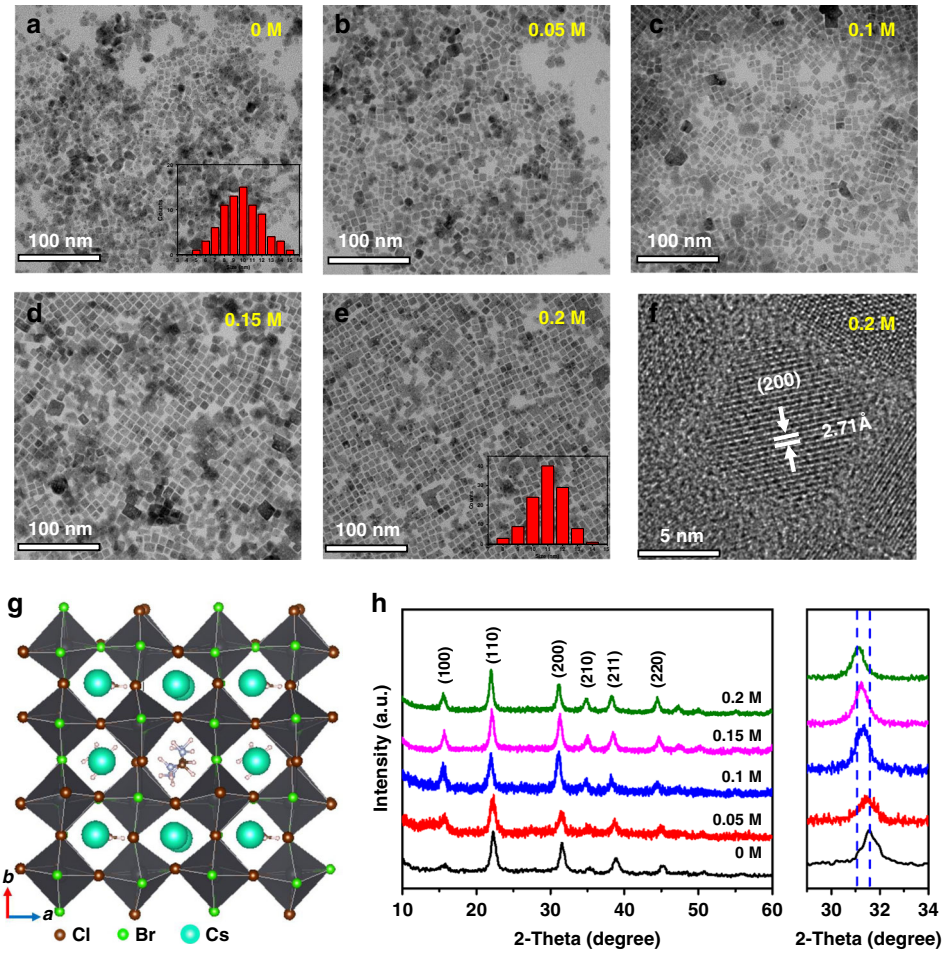

Fig. 1 The structure and morphology of undoped and FA-doped $CsPb(Cl_{0.5}Br_{0.5})_3$ QDs. TEM images of **a** undoped QDs, **b** 0.05 M FA cations adding, **c** 0.1 M FA cations adding, **d** 0.15 M FA cations adding, and **e** 0.2 M FA cations adding. **f** high-resolution TEM images of 0.2 M FA cations adding. **g** the crystal structure graph. **h** XRD patterns of undoped and FA cation doped $CsPb(Cl_{0.5}Br_{0.5})_3$ QDs. The inserts of (**a**) and (**e**) are grain size statistical distributions

pristine QDs, the absorption spectra of FA^+-doped samples (Fig. 2a) exhibit an apparent low energy shift of the excitonic peak from 440 nm to 458 nm, and the shift finally reaches 478 nm for FA^+-only emitters (Fig. S3a), indicating the decrease of QD optical bandgap. For investigating the origin of the bandgap change, firstly we consider the quantum size confinement of QDs, and the influence of sizes on bandgaps can be expressed by the equation[26,27]:

$$\Delta E = \frac{\hbar^2 \pi^2}{2m_r R^2} - \frac{1.786e}{4\pi\varepsilon_0 \varepsilon R} \quad (1)$$

in which m_r, R and ε represent the effective mass of the excitons, the particle radius, and the relative dielectric constant of materials, respectively[28,29]. The calculation results show that the estimated maximum moving of the bandgap are around 16 meV with the particle size changing from 10 ± 0.3 nm in the pristine $CsPb(Cl_{0.5}Br_{0.5})_3$ QDs to 12 ± 0.4 nm in the 0.2 M FA^+ doped $CsPb(Cl_{0.5}Br_{0.5})_3$ QDs, which value is much lower than the experimental change of 110 meV. Therefore, we can deduce that the doped FA cations also contribute to the change of band structure. The PL characteristics for the pristine and FA^+ doped $CsPb(Cl_{0.5}Br_{0.5})_3$ QDs were further explored, as shown in Fig. 2b and Fig. S3. With the ratio of FA^+/Cs^+ increase, the PL peak position show red-shift (from 456 to 473 nm) and finally realize 498 nm for $FAPb(Cl_{0.5}Br_{0.5})_3$ (Fig. S3b).

More importantly, the PL intensity of the 0.2 M doped $CsPb(Cl_{0.5}Br_{0.5})_3$ QDs is obviously enhanced compared with that of pristine QDs. The absolute PLQY is illustrated in Fig. 2c and Fig. S3c, in which the PLQY of FA^+ doped $CsPb(Cl_{0.5}Br_{0.5})_3$ QDs gradually increases and approaches 65% that is 6 times more than the undoped QDs. The PLQY values are listed in Table S1. The increase of PLQY

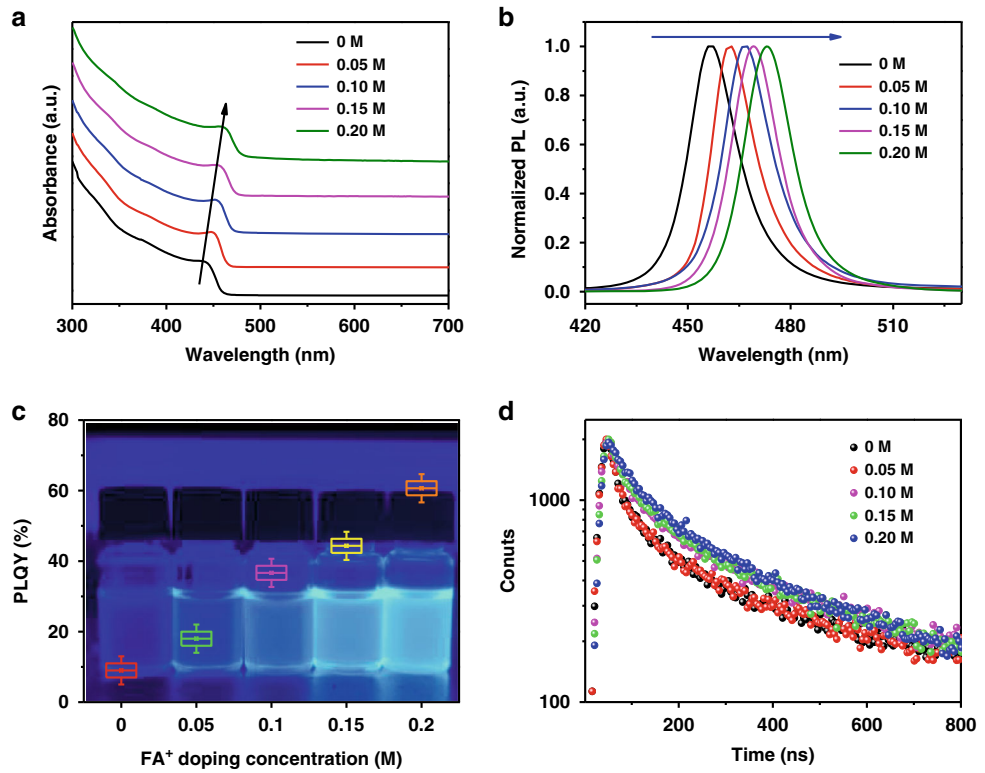

Fig. 2 Photophysical properties of all blue QDs. a absorption spectra, **b** photoluminance spectra, **c** PLQY, **d** TRPL decay curves of FA^+ doped $CsPb(Cl_{0.5}Br_{0.5})_3$ QDs with FA^+ feeding ratio of 0, 0.05, 0.1, 0.15, and 0.2 M, respectively. The background inset of (**c**) shows the picture of the QDs under a UV lamp illumination with 365 nm

primarily comes from the decreased defects in crystal structure by FA doping. To further explore the dynamic origin of the PLQY changing by FA doping, the time-resolved PL (TRPL) spectra for all samples were measured (Fig. 2d and Table S1), and the decay curves were fitted by the biexponential function. The fluorescence lifetimes are about 137.8, 154.6, 183.4, 201.0, and 214.4 ns with FA^+ feeding ratio of 0, 0.05, 0.1, 0.15, and 0.2 M, respectively. The prolonged average lifetime indicates that nonradiative decay channels and defects are suppressed and reduced in doped samples, which improves the radiative recombination of electrons and holes and thus increases the PLQY. As a result, FA doping enhances the exciton binding energy, making excitonic emission dominates in perovskite QDs, which are shown in steady-state and time-resolved photoluminescence spectra. When the FAAC is gradually increased beyond 0.2 M (Fig. S3), the PLQY presents a peak value and then decreases, which is attributed to the excessive FA causing new defects. Simultaneously, the excessive acid in precursor solution results in the agglomeration of QDs[30].

To elucidate the FA cation doping, Fourier transform infrared spectroscopy (FTIR) was conducted in the pristine and treated QD samples. In Fig. 3a, both samples exhibit CH_2 and CH_3 symmetric and asymmetric stretching vibrations between 2840 and 2950 cm^{-1}, and CH_2 bending vibration at 1466 cm^{-1}, which are the representative absorption peaks for hydrocarbon groups[2,31]. For FA-doped perovskites, a strong peak at 1716 cm^{-1} (red area) emerges, which represents the C=N stretching vibration of FA cations[32]. Subsequently, the FTIR curve for the FA-doped perovskites exhibits a broad stretching mode around 3300~3500 cm^{-1} and (pink area), which comes from the N-H stretching vibration. These vibrational peaks are obviously enhanced with the increase of FA cations (see Fig. S4 in the Supporting Information). Above data confirm that FA cations indeed doped into QDs.

We also studied the surface composition of QDs via XPS. The survey spectra of QDs confirm the existence of N, Cs, Pb, Br, and Cl elements (Fig. 3b–f and Fig. S5). Figure 3b and Fig. S5a are the high-resolution spectra of N 1*s*. The peak at 399.8 eV relates to amine groups and it originates from FA cation. The samples exhibits a weak peak at 401.8 eV for N 1*s*, which is attributed to few DDA^+ ions from di-dodecyl dimethylammonium bromide adsorbed onto the QD surface. From Fig. 3c and Fig. S5b, the intensities of Cs 3*d* peaks are significantly weakened

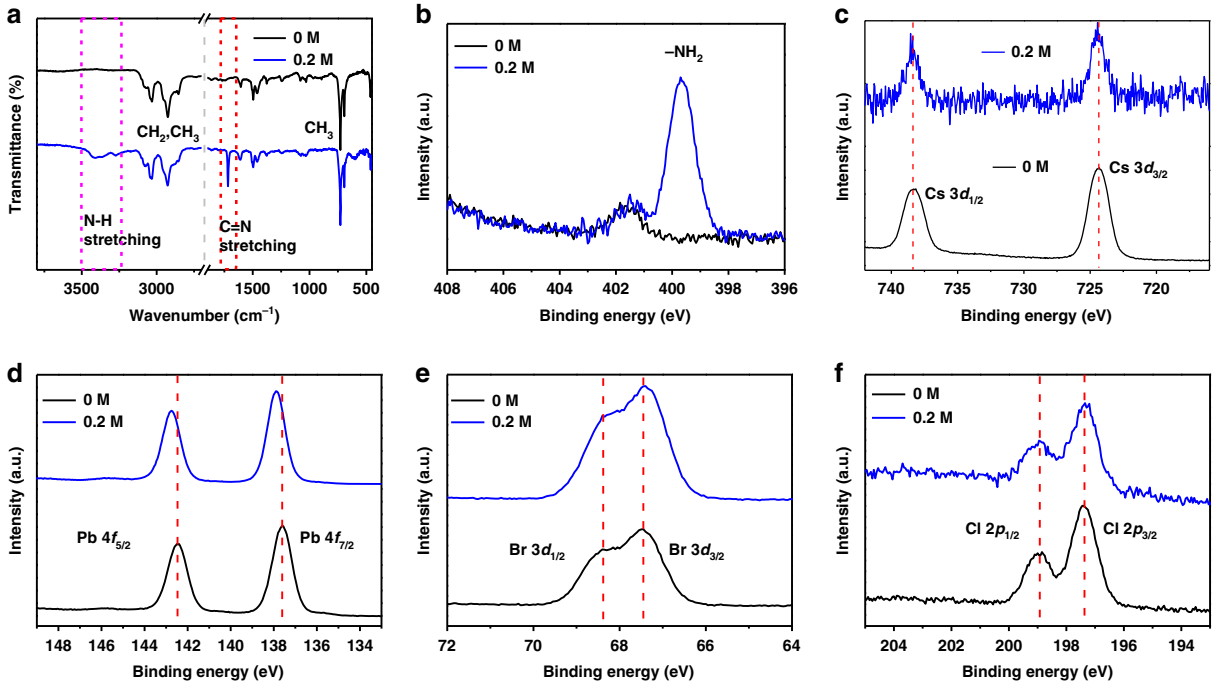

Fig. 3 Chemical analysis of QDs. a FTIR spectra of pristine and FA cation doped QDs. XPS spectra of pristine and FA cation doped, N 1*s* (**b**), Cs 3*d* (**c**), Pb 4*f* (**d**), Br 3*d* (**e**), and Cl 2*p* (**f**)

after FA cation doping. The results further demonstrate that FA cations partially substitute Cs cations into perovskite QDs. Furthermore, the spectra of Pb 4*f* (Fig. 3d) illustrate that the binding energies of Pb $4f_{5/2}$ and Pb $4f_{7/2}$ of the FA-doped sample are higher than those of untreated QDs. The Pb 4*f* peak position moves toward higher binding energy by 0.3 eV, which is attributed to a stronger binding between Pb and halide due to decreased octahedral volume. This also benefits to the stability of crystal structure. For the Cs 6*p*, Cl 2*p*, Br 3*d* core levels, no noticeable change was observed between two samples in high-resolution spectra.

In addition, the femtosecond transient absorption spectroscopy (TAS) was deducted to study the carrier dynamics and the nonradiative recombination process. The transient absorption spectra of samples were characterized under 400 nm excitation (Fig. 4 and Fig. S6). The negative signals represent photoinduced bleaching (PB) originating from the ground-state absorption, which approximate to the excitonic peaks in the absorption spectra. This is associated to the state filling of band-edge excitons (electrons and holes). The positive photoinduced absorption (PA) profiles could be attributed to the hot charge carrier absorption[33]. Comparing to Fig. 4a, Fig. 4b shows slower recoveries and stable PB peak. And for PA of both samples in Fig. 4a, b, TAS shows no contribution of PA in 0.2 M sample, indicating that doped sample process a fast hot charges carriers relaxation[34,35]. In addition, the difference between PB and PA shifts from 100 meV to 50 meV (Figs. 4a, b, and S6a–c) is attributed to the renormalization of the bandgap. Next, the bleaching recovery kinetics of the two samples are depicted in Fig. 4c. It is obvious that the short and ultrafast part is attributed to various trap-assisted nonradiative decay (carrier-phonon scattering, excitons quenching, and Auger recombination) and the improved long part is attributed to excitonic recombination process[36]. To clearly describe the kinetics process in FA cation doped $CsPb(Cl_{0.5}Br_{0.5})_3$ QDs, the carrier recombination mechanism is shown in Fig. 4d. The electrons in the ground states are excited by photons and then transit to the high-energy excited states. The high-energy carriers rapid cool down and reduce the scattering in electron-electron and electron-phonon. From the above investigation, excellent blue-emitting performance is attributed to the following mechanisms: (i) the fast hot charge carriers relaxation and high radiation recombination decrease energy losing; (ii) defect density was decreased to suppress non-radiation decay channel.

Band structure

Furthermore, we explore the influence of FA cation doping on the band structure. Firstly, we estimated the optical band gap (E_g) by Tauc plots extracted from the absorption spectra, as shown in Fig. 5a and Fig. S7. The E_g value for $CsPb(Cl_{0.5}Br_{0.5})_3$ is 2.72 eV, which well matches with those

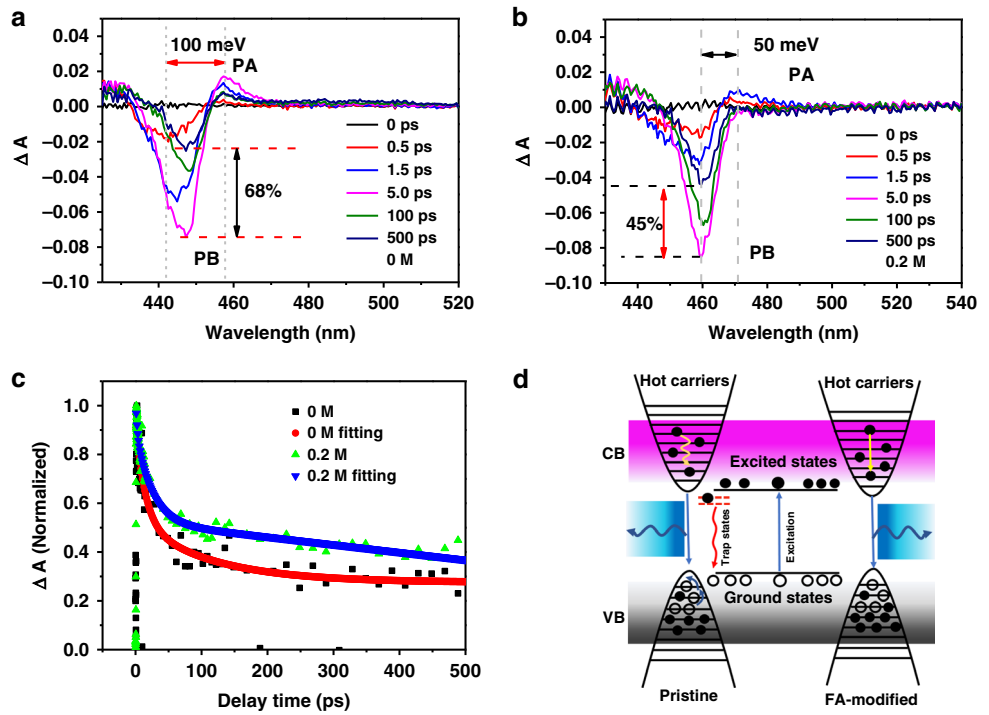

Fig. 4 The carrier recombination dynamic of QDs. Femtosecond transient absorption spectroscopy under 400 nm pump pulse of **a** $CsPb(Cl_{0.5}Br_{0.5})_3$ QDs and **b** 0.2 M FA-doped $CsPb(Cl_{0.5}Br_{0.5})_3$ QDs; **c** the comparison of bleaching recovery kinetics of two samples (λ_{ex} = 400 nm) monitored at their bleaching maximum value; **d** the mechanism of carrier relaxation for excitation above the bandgap

reported elsewhere[37]. And the band gap is 2.60 eV for FA cation doped $CsPb(Cl_{0.5}Br_{0.5})_3$, which is > 0.1 eV larger than the undoped QDs. Furthermore, ultraviolet photoelectron spectroscopy (UPS) was conducted to explore the valence band (VB) edge positions of samples. FA cations could lead to the change of the VB edge of the QDs, as shown in Fig. 5a. The UPS data for all samples are illustrated in Fig. S8. The VB maximum energy (E_{VB}), according to the vacuum level, was calculated to be −5.81, −5.74, −5.67, −5.62, and −5.42 eV for 0, 0.05, 0.1, 0.15, and 0.2 M FA cation doped sample, respectively. The conducting band (CB) minimum energies (E_{CB}) can subsequently be calculated from the E_g and E_{VB} values. Thus, we derived the CB values for 0 and 0.2 M FA^+ doped samples QDs as −2.81 and −3.09 eV, respectively. In addition, Fig. 5c, d show the electronic band structures and the density of states (DOS) of pristine and treated perovskites QDs, which were calculated by the first-principles. The results show that the bandgaps of $CsPb(Cl_{0.5}Br_{0.5})_3$ and FA-doped $CsPb(Cl_{0.5}Br_{0.5})_3$ are very close to each other because both CB and VB are mainly dominated by Pb and halegon ions. In the state density, VB is mainly composed of Br 3*d*, Cl 2*d* and Pb 6*s* electrons states, while CB mainly contains Pb 6*p* electron state. The contribution of Cs and FA cations to CB and VB is negligible. However, the DOS of the doped blue QDs (Figs. 5c, d right) shows that FA cations mainly have an indirect influence on the energy band structure through manipulating halogen bonding orbits with Pb. In addition, the projected density of states (PDOS) on the C, N, H, Pb, Cs, Cl and Br atoms of both samples are computed in Fig. S9. The PDOS illustrates that the individual electronic states of FA cation mainly fill on the deep-level VB. The FA cations widen DOS band, which will cause the delocalization of carrier to decrease energy losing approach in the carrier relaxation process. The result will give a more thorough understanding of the influence of FA cations on the band structure and related carrier injection process in our devices.

Device performance

The excellent photophysical properties of FA cation doping QDs (0.2 M sample) offer exciting prospects for their exploitation in optoelectronic devices. Consequently, we fabricated pure blue LED devices with perovskite QDs acting as light-emitting layer. The schematic device energy alignment is depicted in Fig. 6a.

Band alignment demonstrates that FA cation doped $CsPb(Cl_{0.5}Br_{0.5})_3$ QD-based blue LED has a smaller barrier of hole injection than the undoped device, which changes the hole injection into the emitting layer. Figure 6b shows the voltage-dependent change of luminance and current density for two pure blue QD LEDs. The turn-on voltage (V_{on}) (which is usually specified in literatures as

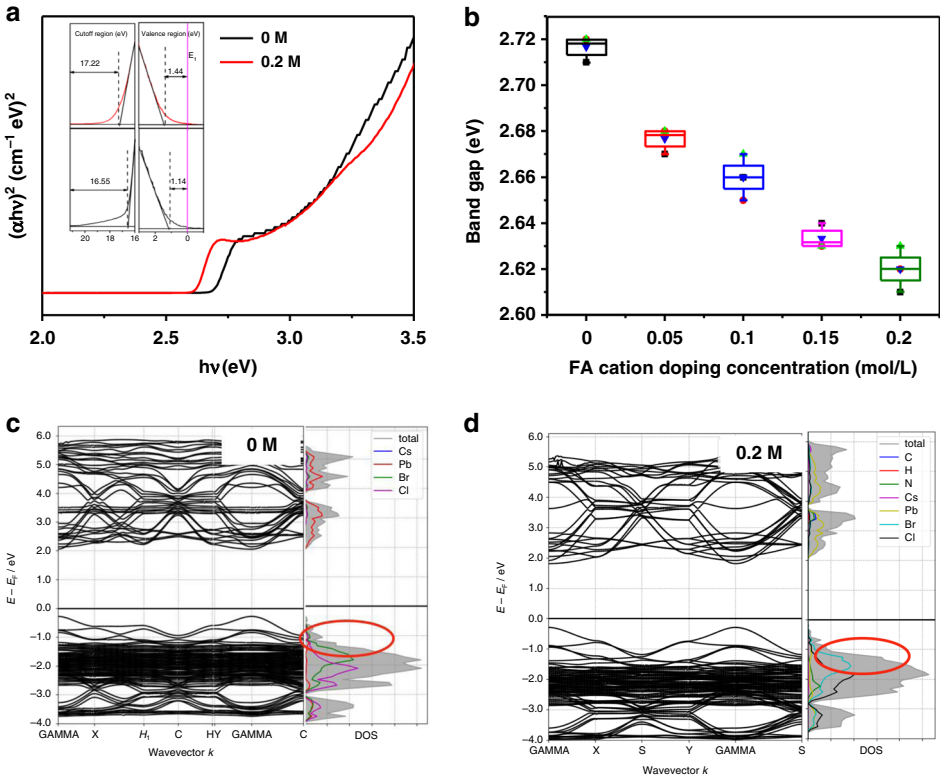

Fig. 5 Electron state filling of QDs. a Tauc plots of pristine and 0.2 M FA cation doped QD films. The inset is UPS spectra of both films. **b** Optical band gap changing with FA cation increase. **c** Left: calculated band structures of pristine $CsPb(Cl_{0.5}Br_{0.5})_3$, and right: corresponding density of states (DOS). **d** Left: calculated band structures of FA cation doped $CsPb(Cl_{0.5}Br_{0.5})_3$, and right: corresponding DOS

the applied voltage can drive luminescence of 1 cd m^{-2}) of FA-doped devices is 2.8 V, slightly smaller than that of undoped device (2.9 V). The current densities of the FA^+ doped devices are substantially lower in the low voltage region. The peak luminance is 1452 cd m^{-2} and 522 cd m^{-2} for devices with and without FA^+ cation doping, respectively. Figure 6c shows normalized EL spectra of two LEDs. Both EL spectra measured at 5 V and the emission wavelength are 457 and 474 nm, respectively. Coupling high luminance with low current density, the current efficiencies of FA-doped $CsPb(Cl_{0.5}Br_{0.5})_3$ QD LEDs show a peak value of 7.4 cd A^{-1}, which is much higher than that of pure $CsPb(Cl_{0.5}Br_{0.5})_3$ (0.31 cd A^{-1}) (Fig. 6d). Notably, the peak EQE is as high as 5.01% (Fig. 6e), which surpasses all previously reported values of pure blue $CsPb(Cl_{0.5}Br_{0.5})_3$ QD LEDs. The efficiencies of LEDs are dramatically improved with the introduction of FA cations (see Fig. S12 in the Supporting Information). The top performances of perovskite blue LEDs in literatures are summarized in Fig. 7 and Table S3, and here we realize the record value (5.01%) in the entire field of pure blue perovskite QD LEDs. The maximum EQE is above 10 times magnitude higher than that of the $CsPb(Cl_{0.5}Br_{0.5})_3$ LED. Here, FA cation doped QDs may possess better band structure to adjust charge balance. And the maximum EQE statistics are summarized in Fig. 6f, which can further illustrate device performance reliability. The high shelf stability of FA-Cs-based QD LEDs can be attributed to the excellent nanocrystals with low defect density and high PLQY. And we use half- lifetime (T_{50}) to judge the device operational stability, which is set as the time needed for the device luminance to decrease to 50% of its initial value (L_0). The T_{50} of the FA-based LED is about 1056 s (Fig. 6g), which is much longer than that of pristine device (150 s). In addition, EL spectrum stability of FA-based LED was measured at different voltages (Fig. 6h), and the results reveal that the QD device keeps a stable emission peak at 474 nm. All detailed parameters are shown in Table 1. And in Fig. 6i a device photo with bright pure blue emission is shown operated under 5 V.

To further investigate the reason of the high performance of LEDs, the surface roughness of the perovskite QD films was charactered by atomic force microscopy (AFM), as shown in Fig. S13. Flat and compact surface was confirmed for the pristine and all doped samples. Good film morphology can reduce the current leakage, which is also an important factor for high performance blue perovskite LEDs. Additionally, the carrier transport

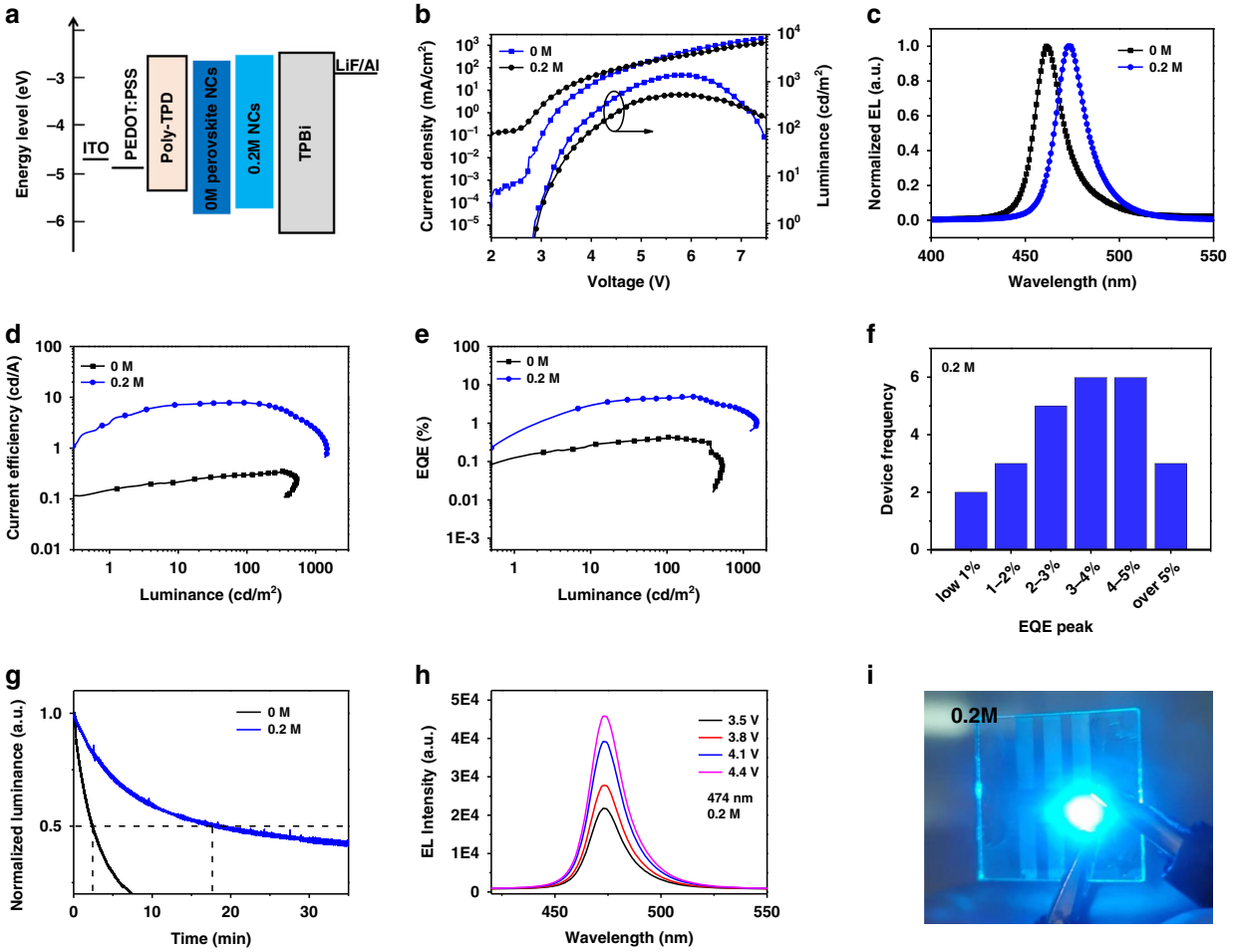

Fig. 6 Blue LED performances based on perovskite QDs. a Schematic band alignment of the LED devices with 0 and 0.2 M FA cation doped QDs. **b** Curves of the current density-voltage-luminance. **c** Normalized electroluminescence spectra of the LED devices with $CsPb(Cl_{0.5}Br_{0.5})_3$ (black curve) and 0.2 M doped $CsPb(Cl_{0.5}Br_{0.5})_3$ QDs (blue curve). **d** Curves of the brightness-current efficiency. **e** Curves of the external quantum efficiency-luminance. **f** The histogram of devices frequency-EQE maximum values in 0.2 M FA cation doped $CsPb(Cl_{0.5}Br_{0.5})_3$ QD LEDs. **g** Emitting stability of two devices. **h** Stable EL spectra of 0.2 M FA-doped sample at different voltages. **i** The photograph of a FA-doped device operating on the voltage of 5 V

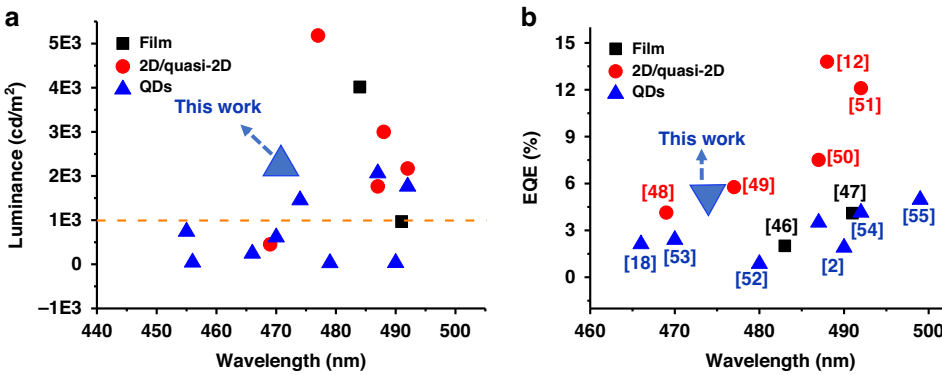

Fig. 7 The development state of blue perovskite LEDs. The blue perovskite LEDs performance statistical graph **a** Luminance-Wavelength data and **b** EQE-Wavelength data. Ref. [46,47] is perovskite film LEDs, Ref. [12,48–51] is 2D/quasi-2D perovskite LEDs, Ref. [2,18,52–55] is perovskite QD LEDs

Table 1 Summary of EL performance of the pristine and FA cation doped blue QD LEDs.

Device	V_{on}[a]	Maximum value		T_{50}[b](s)	Peak @5 V (nm)
		L (cd m^{-2})	EQE (%)		
0	2.9	522	0.44	130	457
0.2 M	2.8	1452	5.01	1056	474

[a] Measured voltage when luminance was 1 cd m^{-2}
[b] T_{50}-time when luminance decrease to 50% of initial value (100 cd m^{-2})

properties of QD LEDs were studied by the "electron-only" and "hole-only" devices, in which current density −voltage (J−V) curves were measured (Fig. S14a, b). The device structures are as follow:

Hole-only: ITO/PEDOT:PSS/poly-TPD/QDs/MoO_3/Al
Electron-only: ITO/PEI/ QDs/TPBi/LiF/Al

The carrier mobility of the QDs was evaluated by fitting the space charges limit current (SCLC) region with Mott −Gurney law[38]:

$$J_{SCLC} = \frac{9}{8}\varepsilon_0\varepsilon_r\mu\frac{V^2}{L^3} \quad (2)$$

in which, ε_0 is the vacuum dielectric constant, ε_r is the relative dielectric constant, μ is the mobility, V is the applied voltage and L is the thickness of the active material. The hole mobilities of undoped and 0.2 M FA cation doped QDs films are 6.24×10^{-6} and 1.32×10^{-4} cm^2 V^{-1} s^{-1}, respectively. The electron mobilities of $CsPb(Cl_{0.5}Br_{0.5})_3$ and FA cation doped $CsPb(Cl_{0.5}Br_{0.5})_3$ QDs films are 3.78×10^{-4} and 8.20×10^{-5} cm^2 V^{-1} s^{-1}, respectively. With the adding of FA cations, the electron mobility decreases while the hole mobility increases, which reveals that the mobilities of two carrier species are more balanced with QD modification and this result agrees with the aforementioned UPS data. In addition, balanced carrier mobility could decline emitting quenching.

Discussion

We successfully realized FA cation doped pure blue $CsPb(Cl_{0.5}Br_{0.5})_3$ QDs at room temperature. The FA cation doping manipulate the morphology and light emission of QDs. It boosts PLQY from 10% to 65% by decreasing nonradiative recombination. The fluorescence lifetime increases 1.6 times than the undoped ones. TAS further elaborates the mechanism of excellent QD emitters originating from fast carrier relaxation and low defects to decrease energy losing channels of QDs. Simultaneously, the first-principle demonstrates that electronic state density of valence band is changed to decline the carrier injection barriers. Ultimately, a champion device was obtained with a high luminance and a peak EQE of 1452 cd m^{-2} and 5.01% at 474 nm, respectively. This work offers a good approach to develop Cl/Br mixed room temperature-synthesized pure blue-emitting perovskite QDs.

Materials and methods

Materials

Cs_2CO_3(99.9%), didodecyldimethylammonium bromide (DDAB,98%), toluene (ACS grade, Fisher), Octanoic acid (OTAc,98%), Formamidine acetate (FAAc, 99%), tetra-octylammonium bromide (TOAB,98%), Methyl acetate (98%), and aluminum (Al) were purchased from Sigma-Aldrich. $PbBr_2$ (99.9%), $PbCl_2$ (99.9%), Poly(3,4-ethylene-dioxythiophene)-poly(styrenesulfonate) dry re-dispersible pellets (PEDOT:PSS (4083)), Poly[N,N'-bis(4-butylphenyl)-N,N'-bis(phenyl)-benzidine (Poly-TPD), 1,3,5-Tris(1-phenyl-1H-benzimidazol-2-yl)benzene(TPBi), and LiF were purchased from Xi'an Polymer Light Technology Corp.

Synthesis and purification FAAc doped $CsPb(Cl_{0.5}Br_{0.5})_3$ QDs

The $CsPb(Cl_{0.5}Br_{0.5})_3$ QDs were synthesized by referencing double ligand-assisted-reprecipitation methods[39] with some modifications. First, cesium precursor was prepared by loading 0.5 mmol of Cs_2CO_3 and 5 mL of OTAc into a 20 mL bottle, and then 0.25 mmol, 0.5 mmol, 0.75 mmol, and 1 mmol FAAc were added and stirred for 20 min at room temperature. 1 mmol mixture of $PbBr_2$ and $PbCl_2$ was added to 50 ml flask. Then, 2 mmol of TOAB and 10 ml toluene were also filled into the bottle to form precursor solution. For the synthesis of pure $CsPb(Cl_{0.5}Br_{0.5})_3$ QDs, 1.0 mL of a Cs^+ precursor solution was swiftly added into 9 mL of a PbX_2 toluene solution. The solution was magnetically stirred for 10 min at room temperature in open air. Subsequently, 3 mL of DDAB (in toluene 10 mg mL^{-1}) solution was added. After 1 min, a volume ratio of 2:1 for ethyl acetate was put into the crude solution; the precipitates were collected separately after centrifugation and dispersed in toluene. The additional ethyl acetate was put into the dispersion solution, and the precipitates were collected and re-dispersed in 2 ml toluene. As for FA-doped QDs, the different mass of FAAc was added into Cs^+ precursor to form mixture A-site cations, and the other processes were the same.

LED fabrication

Pre-patterned indium tin oxide (ITO) glasses with an 8 Ω/square sheet resistance were used as the substrates for the blue QD LEDs. Deionized water, acetone, and isopropanol were used to sequentially clean the ITO substrates. Then the substrates were exposed to UV–ozone ambiance for 5 min at 50 W before sequential coating. The lighting active area of QDs LEDs was 2×2 mm^2. The detailed device structure was ITO/ PEDO:PSS/ Poly-TPD/

QDs/TPBi (50 nm)/LiF (1 nm)/Al (100 nm), which was reported elsewhere[40]. PEDOT:PSS and Poly-TPD were as hole transport layers. PEDOT:PSS was spin-coated and then annealed in air at 120 °C for 20 min to form a 30 nm layer. Next, Poly-TPD film was spin-coated and baked at 120 °C for 15 min in a glove box to form a 20 nm layer. Then $CsPb(Cl_{0.5}Br_{0.5})_3$ and FA cation doped QD solutions were spin coated on the smooth poly-TPD film at 2000 rpm for 60 s, and baked at 50 °C for 10 min to form a 40 nm layer. The remaining layers (TPBi, LiF, Al) were deposited in a thermal evaporator with a pressure of 5×10^{-4} Pa, which deposition rates were 0.2, 0.01, 1 Å s^{-1}, respectively. Film thickness and evaporation rate were controlled by a quartz-crystal sensor.

First-principles calculations

The electron structures of pristine and FA cation doped $CsPb(Cl_{0.5}Br_{0.5})_3$ were conducted using the Vienna Ab initio Simulation Package code[41–43]. The projector augmented wave (PAW) approach and the generalized gradient approximation of Perdew, Burke, and Ernzerhof (PBE) describe the ion-electron interactions and exchange-correlation function[44,45]. For all calculations, the energy cut-off of 520 eV for the plane-wave basis was used with k-points meshes of spacing $2\pi \times 0.03$ Å. All structures were fully optimized until the total energy and residual forces of each atom converged to 10 eV and were smaller than 10 eV $Å^{-1}$, respectively.

Characterization techniques

Transmission electron microscope (TEM, FEI Tecnai F20) were used to study lattice sizes of the perovskite QDs samples. A Bruker D8 X-ray diffractometer which used a copper Kα radiation ($\lambda = 1.54178$ Å) characterized the film X-ray diffraction (XRD). A Cary Eclipse spectrofluorometer show PL spectra of QDs emitter. A PerkinElmer Lambda 3600 UV–vis–NIR spectrometer test ab-sorption curves. Time-resolved PL (TRPL) data were recorded by using the Edinburgh FLS980 spectrofluorometer with a 405 nm laser. PLQY was as well as tested by the same fluorescence spectrometer with an integrating sphere. A Nicolet 6700 FT-IR spectrometer was used to perform Fourier transform infrared spectra (FTIR). The X-ray photoelectron spectroscopy (XPS) was col-lected through ESCALAB 250 X-ray photoelectron spectrometer. A Keithley 2612 source meter connecting with a Newport 818-UV Si photodiode tested current-voltage-luminance characteristics. A NOVA spectrometer recorded EL spectra.

Acknowledgements

J.Q.Z. acknowledges the National Natural Science Foundation of China (No. 61804063), the National Key Research and Development Program of China (No. 2019YFA0705900) funded by MOST., Key Projects of Jilin Province Science and Technology Development Plan (No. 20220201070GX) and the Natural Science Foundation of Jilin Province (No. 20190201208JC). H.-L.Y. thanks the support from the Hong Kong Research Grant Council for the GRF grant (No. 11314122) and research funding from the City University of Hong Kong and the support from Guangdong Major Project of Basic and Applied Basic Research (No. 2019B030302007) and Guangdong-Hong Kong-Macao Joint Laboratory of Optoelectronic and Magnetic Functional Materials (No. 2019B121205002). J.Q.Z. acknowledges H. Wang and Y. Wang for additional TAS test.

Author details

[1]College of Materials Science and Engineering, Key Laboratory of Automobile Materials, Ministry of Education, Jilin University, Changchun 130012, China. [2]Femtosecond Laser laboratory, Key Laboratory of Physics and Technology for Advanced Batteries, Ministry of Education, College of Physics, Jilin University, Changchun 130012, China. [3]Department of Materials Science and Engineering, City University of Hong Kong, Kowloon, Hong Kong, China. [4]School of Energy and Environment, City University of Hong Kong, Kowloon, Hong Kong, China. [5]Hong Kong Institute for Clean Energy, City University of Hong Kong, Kowloon, Hong Kong, China

Author contributions

L.G. designed and finished the experiments. Y.L.Z. contributed to the theoretical calculations. L.J.G., Q.W., and M.W. carried out the opt-physical measurements. J.Q.Z. and Y.H.W. conducted the femtosecond transient absorption measurements. W.T.Z. and J.Q.Z. were responsible for project planning. J.Q.Z., H.L.Y., and L.G. co-wrote the manuscript. All authors have given approval to the final version of the manuscript.

Conflict of interest

The authors declare no competing interests.

Supplementary information The online version contains supplementary material available at https://doi.org/10.1038/s41377-022-00992-5.

Received: 6 March 2022 Revised: 23 August 2022 Accepted: 24 September 2022
Published online: 14 December 2022

References

1. Wang, N. et al. Perovskite light-emitting diodes based on solution-processed self-organized multiple quantum wells. *Nat. Photonics* **10**, 699–704 (2016).
2. Pan, J. et al. Highly efficient perovskite-quantum-dot light-emitting diodes by surface engineering. *Adv. Mater.* **28**, 8718–8725 (2016).
3. Gong, X. W. et al. Highly efficient quantum dot near-infrared light-emitting diodes. *Nat. Photonics* **10**, 253–257 (2016).
4. Cho, H. et al. Overcoming the electroluminescence efficiency limitations of perovskite light-emitting diodes. *Science* **350**, 1222–1225 (2015).
5. Shi, D. et al. Low trap-state density and long carrier diffusion in organolead trihalide perovskite single crystals. *Science* **347**, 519–522 (2015).
6. Lin, K. B. et al. Perovskite light-emitting diodes with external quantum efficiency exceeding 20 per cent. *Nature* **562**, 245–248 (2018).
7. Hassan, Y. et al. Ligand-engineered bandgap stability in mixed-halide perovskite LEDs. *Nature* **591**, 72–77 (2021).
8. Wang, F. Z. et al. High performance quasi-2D perovskite sky-blue light-emitting diodes using a dual-ligand strategy. *Small* **16**, 2002940 (2020).
9. Zhang, F. J. et al. Efficient blue perovskite light-emitting diodes boosted by 2D/3D energy cascade channels. *Adv. Funct. Mater.* **30**, 2001732 (2020).
10. Deng, W. et al. 2D Ruddlesden–popper perovskite nanoplate based deep-blue light-emitting diodes for light communication. *Adv. Funct. Mater.* **29**, 1903861 (2019).
11. Pang, P. Y. et al. Rearranging low-dimensional phase distribution of quasi-2D perovskites for efficient sky-blue perovskite light-emitting diodes. *ACS Nano* **14**, 11420–11430 (2020).
12. Zhu, Z. H. et al. Highly efficient sky-blue perovskite light-emitting diode via suppressing nonradiative energy loss. *Chem. Mater.* **33**, 4154–4162 (2021).
13. Song, J. Z. et al. Quantum dot light-emitting diodes based on inorganic perovskite cesium lead halides ($CsPbX_3$). *Adv. Mater.* **27**, 7162–7167 (2015).
14. Wang, H. C. et al. Perovskite quantum dots and their application in light-emitting diodes. *Small* **14**, 1702433 (2018).

15. Connor, B. A. et al. Alloying a single and a double perovskite: a $Cu^{+/2+}$ mixed-valence layered halide perovskite with strong optical absorption. *Chem. Sci.* **12**, 8689–8697 (2021).
16. Zhang, X. T. et al. Strong blue emission from Sb^{3+} -doped super small $CsPbBr_3$ nanocrystals. *J. Phys. Chem. Lett.* **10**, 1750–1756 (2019).
17. Gangishetty, M. K., Sanders, S. N. & Congreve, D. N. Mn^{2+} doping enhances the brightness, efficiency, and stability of bulk perovskite light-emitting diodes. *ACS Photonics* **6**, 1111–1117 (2019).
18. Pan, G. C. et al. Bright blue light emission of Ni^{2+} ion-doped $CsPbCl_xBr_{3-x}$ perovskite quantum dots enabling efficient light-emitting devices. *ACS Appl. Mater. Interfaces* **12**, 14195–14202 (2020).
19. Pan, J. Y. et al. Multiple cations enhanced defect passivation of blue perovskite quantum dots enabling efficient light-emitting diodes. *Adv. Opt. Mater.* **8**, 2001494 (2020).
20. Bi, C. H. et al. Perovskite quantum dots with ultralow trap density by acid etching-driven ligand exchange for high luminance and stable pure-blue light-emitting diodes. *Adv. Mater.* **33**, 2006722 (2021).
21. Chen, D. Q. et al. Grinding synthesis of $APbX_3$ (A = MA, FA, Cs; X = Cl, Br, I) perovskite nanocrystals. *ACS Appl. Mater. Interfaces* **11**, 10059–10067 (2019).
22. Chen, J. Z. & Park, N. G. Materials and methods for interface engineering toward stable and efficient perovskite solar cells. *ACS Energy Lett.* **5**, 2742–2786 (2020).
23. Philippe, B. et al. Chemical distribution of multiple cation (Rb^+, Cs^+, MA^+, and FA^+) perovskite materials by photoelectron spectroscopy. *Chem. Mater.* **29**, 3589–3596 (2017).
24. Jiang, Y., Wang, X. & Pan, A. L. Properties of excitons and photogenerated charge carriers in metal halide perovskites. *Adv. Mater.* **31**, 1806671 (2019).
25. Feng, W. J. et al. Efficient all-inorganic perovskite light-emitting diodes enabled by manipulating the crystal orientation. *J. Mater. Chem. A* **9**, 11064–11072 (2021).
26. Erol, E. et al. Size-controlled emission of long-time durable $CsPbBr_3$ perovskite quantum dots embedded tellurite glass nanocomposites. *Chem. Eng. J.* **401**, 126053 (2020).
27. El-Ghtami, H., Laref, A. & Laref, S. Electronic and optical behaviors of methylammonium and formamidinium lead trihalide perovskite materials. *J. Mater. Sci. Mater. Electron.* **30**, 711–720 (2019).
28. Mannino, G. et al. $CsPbBr_3$, $MAPbBr_3$, and $FAPbBr_3$ bromide perovskite single crystals: interband critical points under dry N_2 and optical degradation under humid Air. *J. Phys. Chem. C.* **125**, 4938–4945 (2021).
29. Mei, X. Y. et al. Approaching high-performance light-emitting devices upon perovskite quantum dots: advances and prospects. *Nano Today* **43**, 101449 (2022).
30. Yan, D. D. et al. Ultrastable $CsPbBr_3$ perovskite quantum dot and their enhanced amplified spontaneous emission by surface ligand modification. *Small* **15**, 1901173 (2019).
31. Chen, W. W. et al. Surface-passivated cesium lead halide perovskite quantum dots: toward efficient light-emitting diodes with an inverted sandwich structure. *Adv. Opt. Mater.* **6**, 1800007 (2018).
32. Xue, J. J. et al. Surface ligand management for stable $FAPbI_3$ perovskite quantum dot solar cells. *Joule* **2**, 1866–1878 (2018).
33. Luo, C. et al. Ultrafast thermodynamic control for stable and efficient mixed halide perovskite nanocrystals. *Adv. Funct. Mater.* **30**, 2000026 (2020).
34. Mondal, N. & Samanta, A. Complete ultrafast charge carrier dynamics in photo-excited all-inorganic perovskite nanocrystals ($CsPbX_3$). *Nanoscale* **9**, 1878–1885 (2017).
35. Tailor, N. K. et al. Cation-dependent hot carrier cooling in the lead-free bismuth halide $A_3Bi_2I_9$ (a = FA, MA, and Cs) perovskite. *J. Phys. Chem. C.* **125**, 9891–9898 (2021).
36. Mondal, N., De, A. & Samanta, A. Achieving near-unity photoluminescence efficiency for blue-violet-emitting perovskite nanocrystals. *ACS Energy Lett.* **4**, 32–39 (2019).
37. Qaid, S. M. H. et al. Single-source thermal evaporation growth and the tuning surface passivation layer thickness effect in enhanced amplified spontaneous emission properties of $CsPb(Br_{0.5}Cl_{0.5})_3$ perovskite films. *Polymers* **12**, 2953 (2020).
38. Le Corre, V. M. et al. Revealing charge carrier mobility and defect densities in metal halide perovskites via space-charge-limited current measurements. *ACS Energy Lett.* **6**, 1087–1094 (2021).
39. Song, J. et al. Room-temperature triple-ligand surface engineering synergistically boosts ink stability, recombination dynamics, and charge injection toward EQE-11.6% perovskite QLEDs. *Adv. Mater.* **30**, 1–7 (2018).
40. Kumawat, N. K. et al. Blue perovskite light-emitting diodes: Progress, challenges and future directions. Nanoscale **11**, 2109–2120 (2019).
41. Kresse, G. et al. Ab initio molecular dynamics for liquid metals. *J. Non. Cryst. Solids* **192**, 222–229 (1995).
42. Perdew, J. P. et al. Generalized gradient approximation made simple. *Phys. Rev. Lett.* **77**, 3865–3868 (1996).
43. Joubert, D. et al. From ultrasoft pseudopotentials to the projector augmented-wave method. *Phys. Rev. B - Condens. Matter Mater. Phys.* **59**, 1758–1775 (1999).
44. Mortensen, J. J. et al. Real-space grid implementation of the projector augmented wave method. *Phys. Rev. B - Condens. Matter Mater. Phys.* **71**, 1–11 (2005).
45. Zhu, S. et al. Structural, electronic, stability, and optical properties of $CsPb_{1-x}Sn_xIBr_2$ perovskites: A first-principles investigation. *J. Phys. Chem. C* **123**, 20476–20487 (2019).
46. Yuan, F. et al. A cocktail of multiple cations in inorganic halide perovskite toward efficient and highly stable blue light-emitting diodes. *ACS Energy Lett.* **5**, 1062–1069 (2020).
47. Li, J. N. et al. Strontium ion B-site substitution for spectral-stable blue emitting perovskite light-emitting diodes. *Adv. Opt. Mater.* **8**, 2001073 (2020).
48. Shen, Y. et al. Interfacial potassium-guided grain growth for efficient deep-blue perovskite light-emitting diodes. *Adv. Funct. Mater.* **31**, 2006736 (2021).
49. Yan, S. Y. et al. Deep blue layered lead perovskite light-emitting diode. *Adv. Opt. Mater.* **4**, 2001709 (2021).
50. Ren, Z. W. et al. Simultaneous low-order phase suppression and defect passivation for efficient and stable blue light-emitting diodes. *ACS Energy Lett.* **5**, 2569–2579 (2020).
51. Ma, D. X. et al. Chloride insertion-immobilization enables bright, narrowband, and stable blue-emitting perovskite diodes. *J. Am. Chem. Soc.* **142**, 5126–5134 (2020).
52. Hou, S. C. et al. Efficient blue and white perovskite light-emitting diodes via manganese doping. *Joule* **2**, 2421–2433 (2018).
53. Chiba, T. et al. Blue perovskite nanocrystal light-emitting devices via the ligand exchange with adamantane diamine. *Adv. Opt. Mater.* **8**, 2000289 (2020).
54. Shao, H. et al. High brightness blue light-emitting diodes based on $CsPb(Cl/Br)_3$ perovskite QDs with phenethylammonium chloride passivation. *Nanoscale* **12**, 11728–11734 (2020).
55. Zhang, F. J. et al. Stabilizing electroluminescence color of blue perovskite LEDs via amine group doping. *Sci. Bull.* **66**, 2189–2198 (2021).